ORIGINAL ARTICLE

Fast 3D imaging of giant unilamellar vesicles using reflected light-sheet microscopy with single molecule sensitivity

Anita Jannasch[1] ⓘ | **Sven A. Szilagyi[1,2]** | **Moritz Burmeister[1]** | **Q. Tyrell Davis[1,3]** | **Gero L. Hermsdorf[1]** | **Suman De[1,4]** | **Erik Schäffer[1]** ⓘ

[1] Center for Plant Molecular Biology (ZMBP), University of Tübingen, Auf der Morgenstelle 32, Tübingen, Germany

[2] Max Planck Institute for Solid State Physics, Heisenbergstrasse 1, Stuttgart, Germany

[3] School of Life Sciences, University of Dundee, Dow Street, Dundee, Scotland, UK

[4] Sheffield Institute for Translational Neuroscience (SITraN), University of Sheffield, Broomhall, Sheffield, UK

Correspondence
Anita Jannasch, Center for Plant Molecular Biology (ZMBP), University of Tübingen, Auf der Morgenstelle 32, 72076 Tübingen, Germany.
Email: Anita.Jannasch@uni-tuebingen.de

Summary

Observation of highly dynamic processes inside living cells at the single molecule level is key for a better understanding of biological systems. However, imaging of single molecules in living cells is usually limited by the spatial and temporal resolution, photobleaching and the signal-to-background ratio. To overcome these limitations, light-sheet microscopes with thin selective plane illumination, for example, in a reflected geometry with a high numerical aperture imaging objective, have been developed. Here, we developed a reflected light-sheet microscope with active optics for fast, high contrast, two-colour acquisition of z-stacks. We demonstrate fast volume scanning by imaging a two-colour giant unilamellar vesicle (GUV) hemisphere. In addition, the high contrast enabled the imaging and tracking of single lipids in the GUV cap. The enhanced reflected scanning light-sheet microscope enables fast 3D scanning of artificial membrane systems and potentially live cells with single-molecule sensitivity and thereby could provide quantitative and molecular insight into the operation of cells.

KEYWORDS
fluorescence microscopy, light-sheet microscopy, three-dimensional image acquisition

1 | INTRODUCTION

The ability to image and track single molecules in living cells in real time and three-dimensions (3D) represents one of the big challenges in microscopy. A powerful approach to improve the precision of single molecule localization, is to maximize the collection of emitted photons and reduce the background signal from out-of-focus fluorophores. Collection efficiency scales quadratically with the numer-ical aperture (NA) of the imaging objective. Thus, the NA should ideally be as large as possible. Total internal reflection fluorescence microscopy (TIRFM), widely used for single molecule studies, illuminates only a thin plane near the glass–sample interface. This reduction in illumination volume results in a low background and high contrast of single fluorophores. However, due to the intrinsically restricted geometry of illumination, TIRFM is not suitable for 3D imaging of whole cells. To reduce

out-of-focus emissions and achieve a high contrast for 3D imaging, different designs of light-sheet microscopes have been developed.[1–8] Most importantly, the intrinsic optical sectioning reduces phototoxicity, photobleaching and enhances imaging speed compared to a confocal microscope. Therefore, fast 2D and 3D imaging can be realized making light-sheet microscopes a powerful tool for imaging live cells. Traditional light-sheet microscopes (e.g. SPIM) were designed for measuring the real-time dynamics of relatively large samples, such as embryos.[9,10] In these microscopes, the illumination objective is placed perpendicular to the detection objective. However, due to spatial constraints, high NA objectives with an inherent small working distance cannot be used, which limits the resolution and photon collection efficiency. Sub-cellular high-resolution and high-contrast imaging requires a thin light-sheet illumination and the usage of high NA detection objectives. Various optical designs have been developed to enable single-molecule imaging with thin light-sheet illumination.[11,12] Digitally scanned laser light sheets (e.g. a Bessel beam light sheet) improve the uniformity of the light-sheet profile and increase the axial resolution.[13–15] Tilted light-sheet microscopy combines a tilted illumination with long axial range point spread functions.[16] This approach allows 3D super-localization of single molecules. Single objective light-sheet microscopes like oblique plane microscopy and highly inclined laminated optical sheet microscopy use high NA objectives for both illumination and detection[17–21]; and recent developments allow for super-resolution microscopy.[22,23] Other single-objective approaches use reflective surfaces, prisms or micromirrors to create a light-sheet perpendicular to the optical axis[24–28] also allowing 3D localization microscopy in cells. However, these techniques require custom-made sample chambers, may have aberrations due to off-axis illumination and/or imaging or have limited multicolour imaging capabilities. The reflected light-sheet microscope (RLSM) combines thin light-sheet illumination with a parallel arrangement of illumination and detection objectives with super-resolution-imaging capabilities.[29–31] The light sheet is reflected by a small cantilever mirror into a horizontal plane close to the sample surface. This design allows the use of a high NA objective for horizontal sectioning of samples with a light-sheet thickness of about 1 μm, as well as a high NA objective for efficient collection of fluorescence.

We adapted the principle of the reflected light sheet and further developed the design for fast 3D imaging with single molecule sensitivity. Fast 3D scanning of the sample is realized by implementation of active optics allowing the light sheet to be automatically moved through the specimen without moving the sample stage.[32,33] Our implementation enabled the scanning over a volume of 35 × 10 × 15 μm^3 (x, y, z) in less than 500 ms. For simultaneous two colour imaging, we implemented two lasers (488 nm and 561 nm) and dual-view imaging optics. In addition, a 405 nm light sheet was co-aligned for (re-)activation of fluorophores. Thus, potentially, photoactivation experiments with single-molecule 3D super-resolution imaging can be performed.[29,34] As a proof of principle, we here demonstrate the imaging and detection of single fluorophores diffusing in a giant unilamellar vesicle (GUV) and show a fast two-colour, 3D scan of a GUV.

2 | METHODS

2.1 | Design of the reflected 3D scanning light-sheet microscope

The custom-build RLSM is isolated from mechanical vibrations by a simple, custom-built, high-performance vibration isolation system based on steel springs and 3D viscous damping.[35] To avoid drift and diffusive light from any light source other than the illumination source, all adjustments during an experiment are controlled via motorized components from the outside of a dark inner microscope room.[35] The axial and lateral drift of the sample glass surface was determined to be significantly less than 1 nm/s consistent with other microscopes in the laboratory.[36] Thus, active drift control or correction was not necessary. In addition, to visualize the sample, a bright field and interference reflection microscope (IRM Refs. 37, 38;) are included (Figure 1).

2.1.1 | Fluorescence excitation and generation of the thin light sheet

For fluorescence excitation and photoactivation, three diode lasers (405 nm: LuxX 405-120, Omicron-Laserage; 488 nm: LuxX 488-100, Omicron-Laserage; 561 nm: OBIS 561LS-100, Coherent) are collimated and aligned via telescopes (Lens L1, L2, Qioptiq Photonics, Germany), pinholes (PH, 10 μm, Qioptiq Photonics, Germany) and dichroic mirrors (AHF Analysentechnik, Germany). Note that the laser power is significantly reduced by the pinholes. The laser beams are further expanded and focussed by a cylindrical lens (CL, f = 150 mm, Thorlabs) yielding a line profile in the back focal plane of the high NA, water dipping illumination objective (Objective 1, CFI Apo NIR 40× W, 0.8 NA, Nikon, Japan). The cylindrical lens is placed on a motorized rotation mount (SR-7012-S, SmarAct, Germany) allowing different orientations of the light sheet. To control the thickness and width of the light sheet, two irises, IR1 and IR2, are employed, respectively. After passing the illumination objective, the thin light sheet is reflected by a tipless gold-coated atomic-force-microscopy
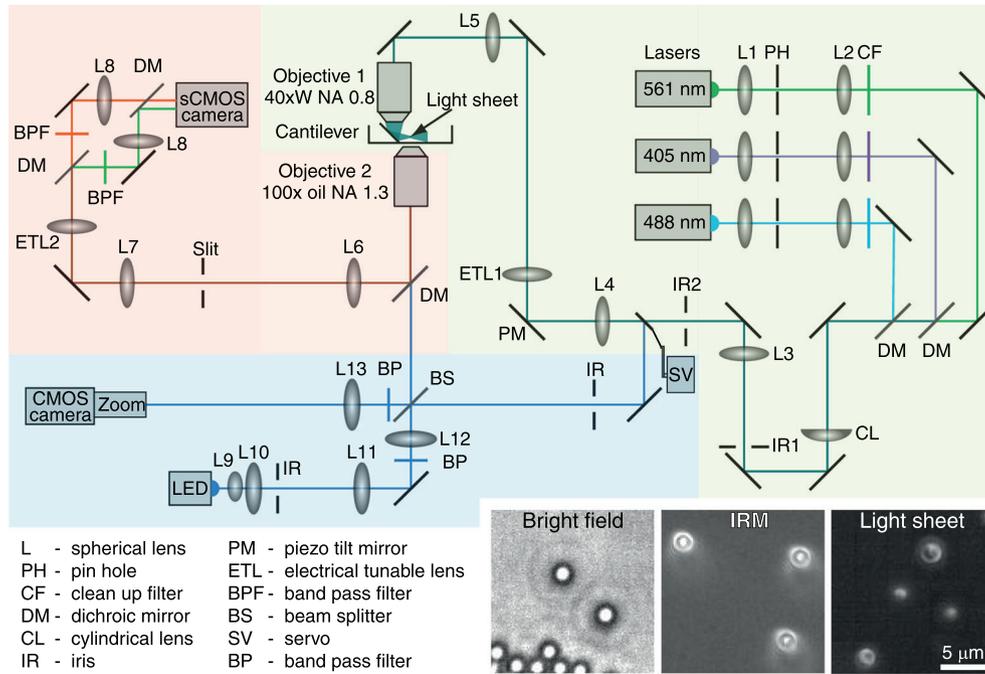
FIGURE 1 Schematic of the reflected 3D scanning light-sheet microscope design. Shown are the fluorescence excitation and generation of the thin light sheet (light green box), the fluorescence detection path (light red box), and the interference reflection microscopy and bright field illumination path (light blue box). The optical path is drawn to scale. Focal length of lenses L1–L13 in mm are: 25, 100, 100, 100, 200, 160, 80, 250, 20, 40, 80, 300, and 200, respectively. Inset: bright field, IRM, and light-sheet image of 2 μm-diameter fluorescently coated microspheres

cantilever (HYDRA2R-100NG-TL, AppNano, USA). The backside of this cantilever acts as a mirror reflecting the light sheet by 90° parallel to the imaging plane. The cantilever is attached to piezo positioners (SLC-1720, SR-7012, SmarAct, Germany) that enable 3D movement as well as rotation around the illumination objective. In this manner, an object of interest can be illuminated from a desired orientation. In addition, a piezo tilt mirror (PM, TT2.5, Piezoconcept, France) is placed in the conjugated plane of the back focal plane of the illumination objective (Objective 1) enabling fast movement of the reflected light sheet in the z-axis of the sample plane. An electrically tunable lens (ETL1, EL-10-30-C-VIS-LD, Optotune, Switzerland) is used to adjust the focus position of the light sheet relative to the cantilever mirror and sample of interest. The piezo motors and ETLs are controlled via LabView (National Instruments, Austin, TX, USA).

2.1.2 | Fluorescence detection

The fluorescence emission is collected by a high NA oil immersion objective (Objective 2, CFI S Fluor 100× Oil, 1.3 NA, Nikon, Japan) and imaged onto a sCMOS camera (ORCA-Flash4.0 V2, Hamamatsu, Japan). With the overall magnification, the image pixel size corresponded to

26 nm. To increase the pixel size and field of view, the magnification could potentially be reduced by using shorter focal length lenses L8. Note that a reduction of the beam diameter by the telescope composed of lenses L6 and L7 by a factor two was necessary to prevent clipping of the beam by the subsequent ETL2. Such clipping was associated with a loss of resolution. With the second ETL (ETL2, EL-16-40-TC-VIS-5D, Optotune, Switzerland), the z position of the image plane inside the sample above the detection objective can be adjusted. Note that both ETLs are mounted with their optical axis parallel to the gravitational acceleration vector. Simultaneous image acquisition of two colours is realized by image-splitting optics (dichroic mirror DM, band pass filter BPF, Lens L8) placed in front of the camera[37]. Through individual placement of Lens 8, the colour splitter also allows adjustment to colour-specific focal planes. The lasers and the camera are triggered and controlled via μManager.[39]

2.1.3 | Interference reflection and bright field microscope

For the LED-based IRM[37], an image of the LED (450 nm Royal-Blue LUXEON Rebel LED, Lumileds, Germany) is magnified by two telescopes (Lens L9-12) and projected

into the back focal plane of the detection objective (Objective 2). The detection and illumination light paths are separated by a 50/50 beam splitter plate (BS, F21-000, AHF Analysentechnik, Germany). A tube lens (Lens L13) and a zoom (S5LPJ7073, Sill Optics, Germany) magnify the sample image about 70× and project it onto a CMOS camera (Lt225, Lumenera, USA). Additionally, the LED is used for bright field illumination by coupling the light via the BS and a movable mirror that is mounted on a servo and can be switched in and out of the illumination path of the light sheet. Thus, while IRM and light sheet–based imaging can be done simultaneously, brightfield microscopy is only possible without light sheet illumination. In the setup, brightfield microscopy is useful for initial alignment of the cantilever.

2.2 | Preparation of GUVs and supported lipid bilayers

The GUVs were prepared using established protocols for electroformation.[40,41] Briefly, 2 μl of a lipid mixture (99.95 mol% DOPC, 0.044 mol% DiO (3,3'-dioctadecyloxacarbocyanine perchlorate), 3×10^{-7} mol% rhodamine-PE) in chloroform were pipetted on each of the two platinum wires in the lid of a custom-made chamber made out of polytetrafluoroethylene. The lipid mixture was dried under vacuum for 10 min and the chamber filled with 350 μl of a 300 mM sucrose solution. The lid was screwed on the chamber and the platinum contacts were connected to a function generator (H-Tronic, FG 250 D). For electroformation of GUVs, we used a frequency of 10 Hz with a 2 V amplitude over a time of 60 min. Release of GUVs from the electrodes was achieved with a frequency of 2 Hz and 2 V amplitude for 30 min. Before experiments, the glass surface of a glass bottom Petri dish (ibidi, μ-Dish 35 mm) was blocked with 50 μl BSA (18 mg/ml). Afterwards, the Petri dish was filled with 1 ml of a 310 mM glucose solution supplemented with an oxygen-scavenger system (20 μg/ml glucose oxidase, 8 μg/ml catalase). Finally, the sucrose GUV solution was added and allowed to settle to the glass surface for approximately 30 min. The supported lipid bilayers were prepared using vesicle deposition.[42,43] The lipid mixture and dye ratio were the same as for the GUV preparation.

2.3 | Data acquisition and analysis

For light-sheet characterization, a mixture of 1 μg/ml fluorescein and 1 μg/ml tetramethylrhodamine in 2 ml Milli-Q water was used. Images were acquired using 2×2 binning of the sCMOS camera resulting in an effective pixel size of 52 nm. The exposure time (10–100 ms) and the laser power (1–100 mW) were varied to find an optimal balance between signal intensity and temporal resolution. For all images, background images were taken and subtracted. The images were analyzed using the image processing package Fiji.[44] Experiments were carried out at room temperature (25 °C). For additional test images, we used 2 μm-diameter polystyrene microspheres (Bangs Laboratories, Fishers, USA) incubated with green fluorescent protein.

For tracking of single fluorophores, the Trackpy (v0.4.1) package for Python was employed.[45] The Gaussian spot localization in the GUV images was carried out with a spot diameter of 9 pixels and minimal integrated brightness of 150 counts. The detected features in each image were then linked to subsequent ones in the image stack with a maximum travel distance of 10 pixels per frame and at most five skipped frames. The resulting trajectories were filtered to have a length of at least 30 frames or more.

The 3D model of the GUV was reconstructed via the 3D Viewer plugin in Fiji with a threshold of 50 and a resampling factor of 4 for the surface plot and a resampling factor of 1 for the volume plot.[44]

3 | RESULTS AND DISCUSSION

3.1 | Characterization of the light sheet

The light-sheet setup enables fast 3D imaging of GUVs and single cells using a thin light sheet reflected by a gold-coated atomic-force-microscopy cantilever placed next to the sample of interest. The custom-built setup is schematically illustrated in Figure 1 and described in detail in Section 2. To quantify the optical properties of the light sheet, we either imaged the lasers directly or excited a fluorophore solution using the rotatable light sheet with and without cantilever (Figure 2, see Section 2). By projecting the light-sheet focus into the image plane of the high NA detection objective without the cantilever, fluorophores and emission filters, we could directly image the cross section of the lasers that form the light sheet and confirm that all three lasers were coaligned (Figure 2(A)). Using Iris 2 (Figure 1), we adjusted the width of the light sheet to match the width of the cantilever (35 μm). By inserting the cantilever mirror, the light sheet is reflected into a plane coinciding with the imaging plane. Using a fluorescent solution excited by the 488 nm and 561 nm lasers (Figure 2(B)), we could verify both the width and even illumination of the excited region.

To determined the thickness of the light sheet during normal imaging, we rotated the cylindrical lens by 90 degrees and imaged the excited cross section normal to the plane of the light sheet (Figure 2(C)). The
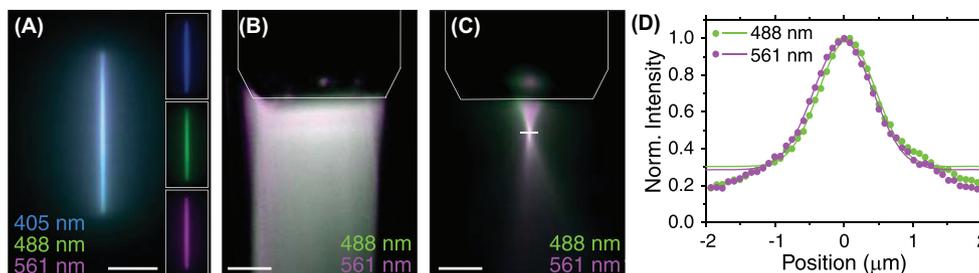
FIGURE 2 Characteristics of the light sheet. (A) Cross-section image of the three co-aligned lasers forming the light sheet without cantilever. Insets show the individual laser cross sections. (B,C) Images of excited two-colour fluorescent solution using the cantilever-reflected light sheet. In (C) the cylindrical lens was rotated by 90° resulting in a 90° rotated light sheet viewed from the side. The tip of the cantilever is marked by thin white lines. Scale bar: 10 μm. (D) Intensity profiles (circles) of the beam waists (white line in (C)) for the 488 nm and 561 nm laser fitted with Gaussian functions (lines, fit region: $\pm 1.3 \mu$m)

intensity distribution of the most narrow light-sheet cross section was then analyzed by fitting Gaussian functions ($I_0 \exp(-2x^2/\omega_0^2) + I_b$) through the cross sections, where ω_0 is the thickness of the light sheet and I_b is the intensity of the background signal (Figure 2(D)). The measured profiles were well-described by the Gaussians and showed that the light-sheet thickness was less than 1 μm for both excitation wavelengths (FWHM$_{488\,nm}$ = 890 nm and FWHM$_{561\,nm}$ = 940 nm). Since for this measurement the light-sheet plane was perpendicular to the image plane, there was some background fluorescence from fluorophores excited above and below the image plane. This out-of-focus contribution—not present when the light-sheet plane coincides with the image plane—explains the deviations from a Gaussian at a larger distance from the centre. These deviations could be modelled by a constant offset. The total field of view was determined by the width of the cantilever (35 μm) and length of the light sheet. The length can be approximated to be 2× the Rayleigh length or about 10 μm. By changing the dimension of the incident laser beams with Iris 1, the thickness (FWHM) of the light sheet can be increased up to 2.5 μm resulting in an increased light-sheet length of up to 50 μm. Alternatively, since we use an illumination objective with a fairly high NA of 0.8, the light sheet can also be decreased in thickness resulting in a shorter Rayleigh length.[29] The focus position of the light sheet, that is, its most narrowest point, can be adjusted laterally using the electrically tunable lens ETL1. Overall, the reflected light-sheet dimensions are comparable to previous ones[29] and can be varied in a certain range according to the application.

To illustrate and compare the three different microscopy modes, we imaged 2-μm-diameter microspheres coated with a fluorophore (inset of Figure 1). Bright-field and IRM images were taken of surface immobilized microspheres and the light-sheet image of freely diffusing ones. For the latter, microspheres either appeared as open or smaller solid circles. We attribute the intensity distribu-

tions to cross sections of microspheres illuminated at different heights. Since the fluorophore was only on the surface of the microspheres, microspheres illuminated at their equator appear as rings and others illuminated closer to their top or bottom appear as smaller solid circles indicating that hardly any out-of-focus light contributed to the image. Note that since the bright-field and light-sheet mode are exclusive, we usually used the bright-field microscope mode only for initial positioning of the cantilever.

3.2 | Tracking of single molecules in GUV membranes

To demonstrate single-molecule sensitivity and the high contrast of the RLSM, we measured the diffusion coefficient of fluorescent lipids (rhodamine-PE) in a GUV (Figure 3). Since the diffusion of these lipids was limited to the spherical membrane surface of the GUV, we positioned the light sheet at the top of the GUV about 10 μm away from the glass surface. In this manner, the detected diffusion is approximately limited to the GUV cap and two dimensions. At a sufficiently low concentration of fluorescently labelled lipids, single near diffraction-limited spots and their diffusive motion could be imaged (Figure 3(A), see Video 1). The images were acquired at a rate of 67 frames/s (15 ms per frame) allowing to track single spots (Figure 3(B)). From the trajectories, we calculated the ensemble-averaged mean squared displacement (MSD, Figure 3(C)). A least-square linear fit ($4D\tau + \epsilon$) resulted in a diffusion coefficient D of 1.63 $\pm$ 0.03 μm^2/s. Since the diffusion coefficient is consistent with literature values[46] and tracked spots were approximately diffraction-limited and sufficiently far apart, we conclude that we tracked single lipids. We could not detect single-molecule bleaching steps because molecules were not stationary. The parameter $\epsilon = 4\sigma^2$ was 0.114 $\pm$ 0.007 μm^2 corresponding to a localization uncertainty σ of 170 $\pm$ 40 nm.[47] Since molecules diffuse a
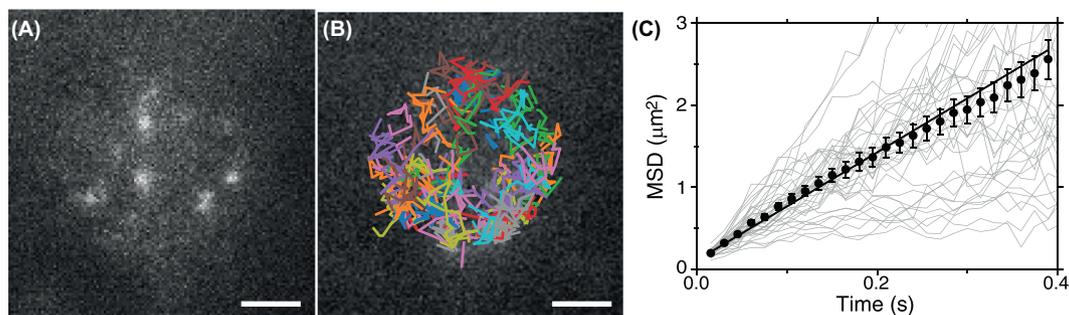
FIGURE 3 Single molecule detection of lipids diffusing in the spherical cap of a GUV. (A) Image of the GUV cap showing single lipid molecules (rhodamine-PE, see Video 1). Scale bar: 2 μm. (B) Single-molecule tracks. (C) Mean squared displacement (MSD) of the single traces ($N = 39$, light grey) detected in (B). Ensemble average MSD (black symbols) with standard error of the mean (SEM) and weighted linear fit
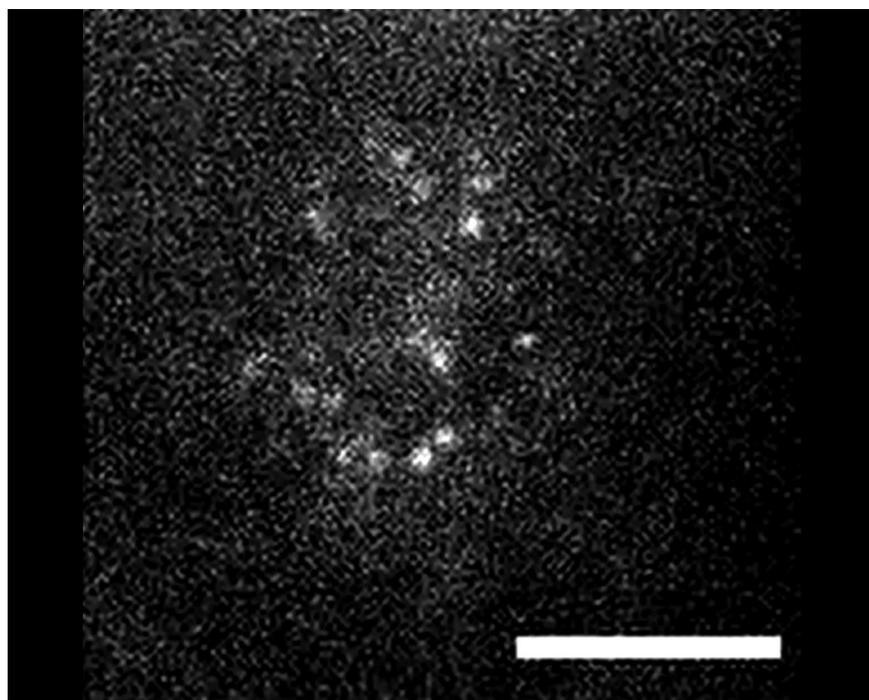

VIDEO S1 Movie of fluorescent lipids (rhodamine-PE) diffusing in the cap of a GUV. The tracked lipids are shown in Figure 3(B). Movie frame rate: 3.5x slower than real time. Scale bar: 2 μm (laser output power: 100 mW, λ: 561 nm, frames: 500, exposure time: 15 ms).

significant distance during the integration time of a single frame, we expect the localization precision to be smaller for stationary molecules. As a control measurement, we measured the MSD of the same fluorescent lipids diffusing in a supported lipid bilayer using TIRFM (data not shown).[43] The resulting diffusion coefficient was about 0.15 μm^2/s. This coefficient is roughly 10× smaller compared to the one we measured in GUV caps, but is in agreement with previous work that showed that under identical conditions the lipid diffusion coefficient in GUVs is much larger than in supported lipid bilayers of identical composition.[46] Since the solid support influences the dynamics of the lipid bilayers, GUVs are a more realistic model to study the dynamics in membranes.[48] Additionally, it was shown that the diffusion coefficient of membrane proteins does not only depend on the protein size and the viscosity of the mem-

brane and surrounding medium but also on the membrane shape and tension.[49] Therefore, it is important to provide a tool that can resolve the spatial and temporal dynamics of single membrane proteins on free-standing lipid bilayers. In summary, the imaging contrast was high enough to enable single-molecule studies at micrometre distances from a glass surface.

3.3 | Fast 3D scanning

Axial scanning of the light sheet using active optics enables fast 3D imaging without moving the sample or the objectives (Figure 4). The imaging speed is mainly limited by the integration time of the camera. For fast scanning of the light sheet through the sample, we implemented a piezo
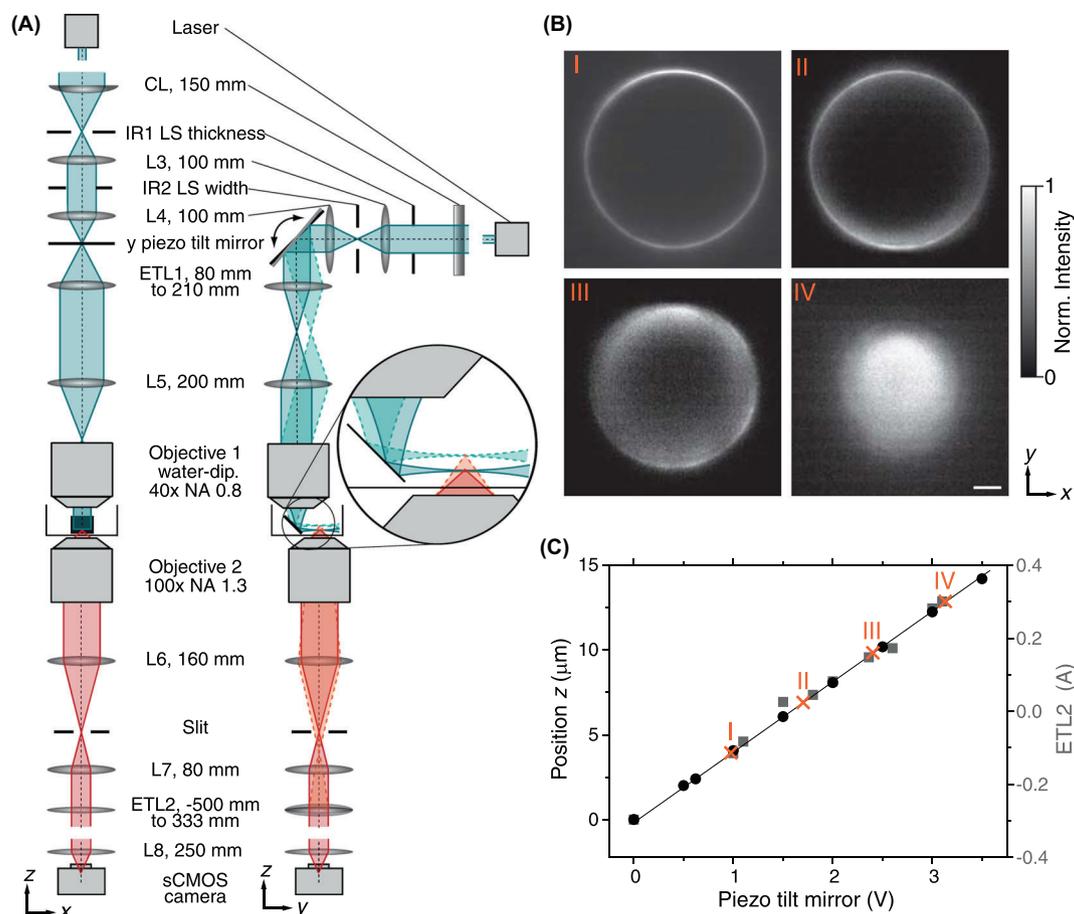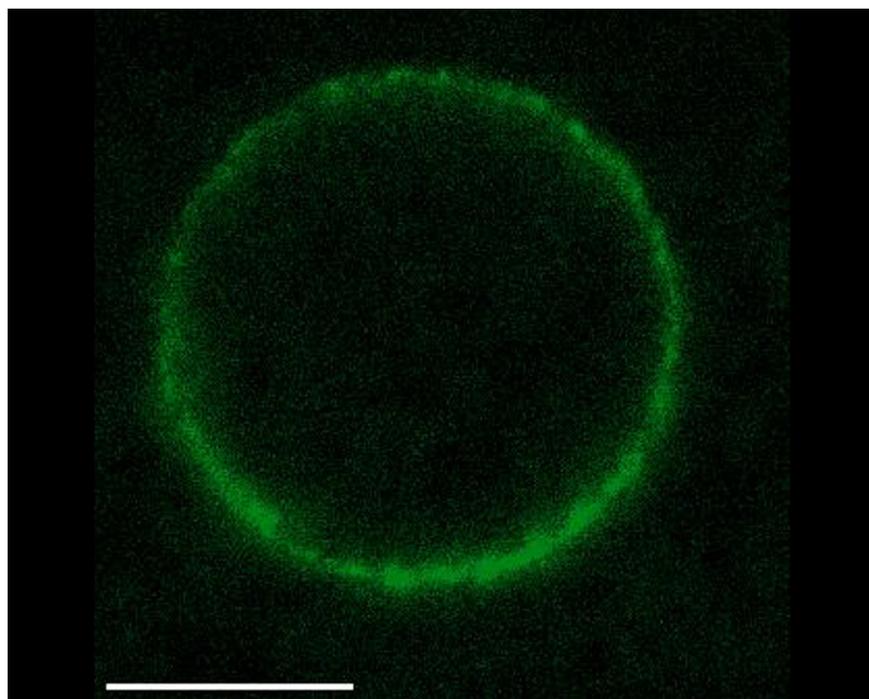
FIGURE 4 Active optics calibration for 3D imaging. (A) Schematics illustrating the two planes normal to the orientation of the optical axis, the x–z and y–z plane, respectively. A tilt of the piezo mirror results in a y-axis translation of the light sheet in the sample. The cantilever mirror converts this lateral y-motion to a vertical z shift of the light sheet. At the same time, an electrically tuneable lens, ETL2, is employed to adapt the image plane of the detection objective. (B) Images of a GUV, labelled with DiO, at different z-positions. Scans were carried out with a theoretical step size Δz of 3 μm. Scale bar: 5 μm (laser output power: 100 mW, λ: 488 nm, exposure time: 25 ms). (C) Calibration of z-scan parameters. The z position of the light sheet (black symbols, left axis) depended linearly on the applied voltage on the piezo tilt mirror. Additionally, the z position of the detection plane depended linearly on the focal length and current of the ETL2 (grey symbols, right axis). To match the light sheet plane with the image plane, both the piezo tilt mirror and the ETL2 were moved with a constant relative factor of 0.2 (A/V). I, II, III and IV correspond to the images in (B)

tilt mirror in a conjugate plane to the back focal plane of the illumination objective (Figure 4(A)). By tilting the piezo mirror, the laser beams will be displaced laterally in the sample. The cantilever mirror converts this lateral displacement to an axial variation of the excitation plane (z-axis). To match the imaging plane of the camera with the z position of the light sheet, we employed an electrically tunable lens (ETL2 in Figures 1 and 4(A)). For fast imaging, this tunable lens needs to be synchronized with and matched in calibrated z-motion amplitude to the piezo tilt mirror. As a test sample with a defined geometry, we chose a spherical, fluorescently labelled GUV. To image GUV cross sections, we applied a certain set point voltage to the piezo tilt mirror illuminating only a defined plane of the GUV. Then, we adjusted the current of the tuneable lens until the cross section was in focus. We repeated this

process for different set point voltages and, in this manner, recorded a stack of cross sections at different z positions of the GUV (Figure 4(B)). Because of the spherical geometry, we could calculate the difference in height between the individual cross sections from their respective radii. Thus, we could calibrate both the piezo tilt mirror and tuneable lens and synchronize their motion. Calibration revealed that the image z position depended linearly on both the voltage of the piezo tilt mirror as well as the current of the tuneable lens (Figure 4(C)). This linear dependence facilitated an easy and fast automatic scanning of the sample by simultaneous adjustment of both the voltage of the piezo tilt mirror and current of the tuneable lens. The response time of the piezo tilt mirrors (2 ms) and the electrically tunable lens (10 ms), and the minimal integration time of the camera (5 ms, for 2 × 2 binning) were fast enough so that
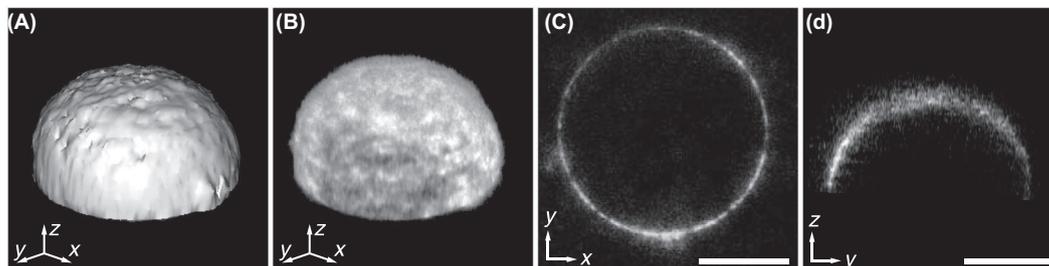
FIGURE 5 3D scan of a GUV (Ø 23 μm) labelled with DiO and rhodamine-PE. (A) Reconstructed surface plot, (B) volume plot of the acquired z-stack, (C) x–y and (D) x–z cross-section of the GUV shown in (A,B). For reconstruction only the red-channel (rhodamine-PE) was used. Scale bar: 10 μm (laser output power: 100 mW, λ: 561 nm, scan height: 11 μm, frames: 44, step height: 0.25 μm, exposure time: 15 ms)

VIDEO S2 One-colour (red-channel, rhodamine-PE) z scan through a DiO and rhodamine-PE labelled GUV that was used for the 3D reconstruction shown in Figure 5. The colour code represents different z heights. Scale bar: 10 μm. Movie frame rate: 4.5x slower than real time (laser output power: 100 mW, scan height: 11 $\mu\mu$m, frames: 44, step height: 0.25 μm, exposure time: 15 ms).

the acquisition rate was limited solely by the photon budget of the sample.

To demonstrate fast, simultaneous two-colour 3D imaging, we scanned through the hemisphere of a GUV labelled with both a fluorescent lipid and a membrane dye, rhodamine-PE and DiO, respectively, that were simultaneously imaged in the red and green channel (Figure 5, see Video 2 and 3). The GUV diameter was $\approx$ 23 μm. Although the length of the light sheet was only $\approx$10 μm, the image stack, recorded in 660 ms, could be used to reconstruct the 3D GUV structure. The reconstruction clearly shows the spherical shape of the GUV (Figure 5(A), (B)). Deviations from sphericity we attribute to the short Rayleigh length of the light sheet. A cross section through the 3D reconstructed GUV also demonstrates the high SNR and low amount of out-of-focus fluorescence (Figure 5(C), (D)). The scan was recorded with a step height Δz of 0.25 μm, which is roughly 4× smaller than the light-sheet

thickness (FWHM). In principle, 2× faster scanning could be achieved by increasing the step height to one half of the light-sheet thickness in accordance with the Nyquist-Shannon sampling theorem. The exposure time for each frame was 15 ms, sufficiently short to observe the diffusion of single fluorescent lipids in the cap (see Video 1). Note that in Figure 5, the fluorescent lipid concentration was 10× higher compared to Figure 3. Therefore, single molecules could not be tracked, but regions of higher and lower fluorophore density can be seen. After scanning the GUV for a second time, we did not observe any change in the fluorescent intensity, yet (data not shown), indicating that the thin light sheet in combination with fast scanning also minimizes photobleaching. Overall, the synchronized and calibrated active optics allowed for fast, simultaneous 3D imaging of two colours with single-molecule sensitivity.

While the ETL2 was sufficiently fast to shift the detection focal plane and follow the illumination plane, its

VIDEO S3 Two-colour *z* scan through the GUV shown in Figure 5. The GUV was labelled with two dyes (magenta: rhodamine-PE, green: DiO) and simultaneously excited with 488 nm and 561 nm. The two colours were imaged on the sCMOS camera at the same time. Movie frame rate: 4.5x slower than real time. Scale bar: 10 μm (laser output power of both lasers: 100 mW, scan height: 11 μm, frames: 44, step height: 0.25 μm, exposure time: 15 ms).
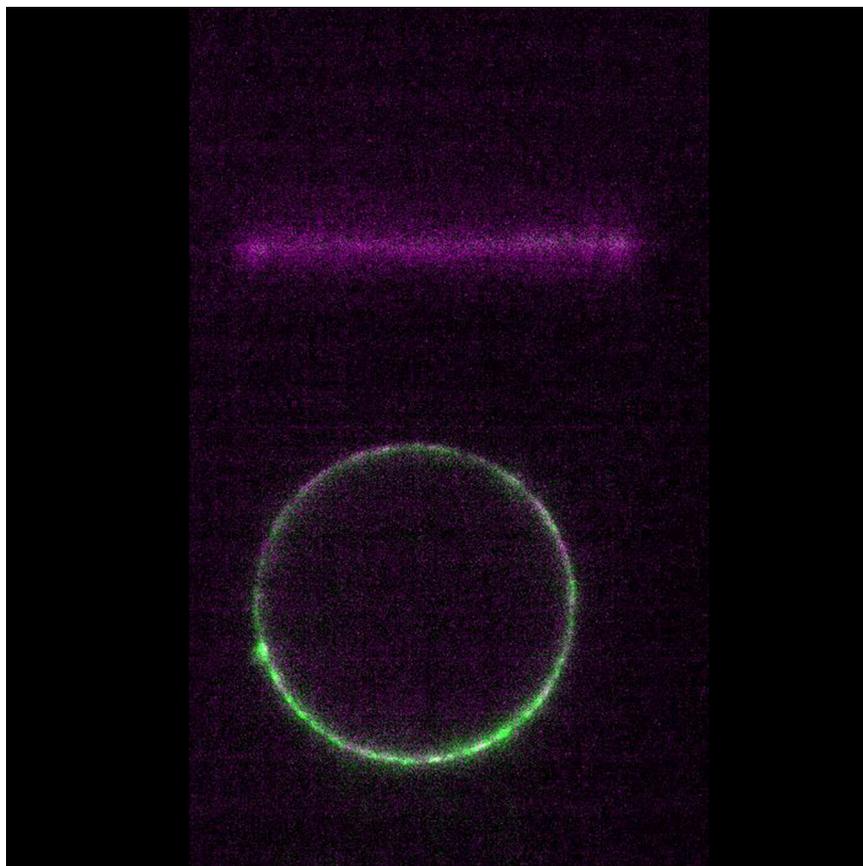
quadratic defocus is not sufficient for an aberration-free defocus when using a high-NA objective.[32,50–52] Also, since we used an oil-immersion objective and image about 10–20 μm away from the surface, we had significant spherical aberrations from the glass–water interface and different sugar solutions inside and outside the GUV. In principle, all of these aberrations could be corrected for by additional adaptive optics.[52] In general, the defocus and/or change of the tube length can also compensate part of the spherical aberrations.[53,54] Another simple compensation approach is to use a different refractive index for the immersion oil.[55] However, since contrast was sufficient to track single molecules, we did not further characterize or minimize aberrations.

4 | CONCLUSION

In this study, we presented an RLSM optimized for fast 3D two-colour imaging. The combination of a thin light sheet (< 1μm) and a high NA detection objective allowed us to image and track the diffusive motion of single lipid molecules in a GUV cap. Fast 3D imaging is achieved by implementation of a piezo tilt mirror for *z*-scanning of the light sheet and an electrically tunable lens for focus adjustment. Calibration and synchronization of the active optics

allowed fast automatic scanning of samples. Faster scanning could be achieved by choosing a smaller region of interest on the camera for recording. The overall volume scan rate is a compromise between the number and distance between image planes, that is, the total *z* height, camera exposure related the available laser power, the number of pixels read-out from the camera, that is, the field of view and the scanning speed of the active optics. Here, we used fixed increments for a new *z* position. We expect that the scanning speed can be increased by continuously varying the *z* position. Also, an optimized input signal for the electrically tunable lens may speed up the scanning process significantly.[56] Overall with the current implementation, 3D image stacks can be recorded sufficiently fast to investigate the complex dynamics inside single cells in the future. Moreover, due to the implementation of the 405 nm laser, photoactivation experiments are feasible. Thus, this method has great potential for super-resolution imaging and 3D tracking of single molecules in living cells on a millisecond time scale.

AUTHOR CONTRIBUTIONS

E.S. and A.J. designed research; M.B., S.A.S., Q.T.D., G.H., S.D. and A.J. built and designed the microscope setup; A.J., S.A.S. and M.B. performed measurements; A.J. and E.S. wrote the article.

CONFLICT OF INTEREST

The authors declare that there are no conflicts of interest related to this article.

ORCID

Anita Jannasch ![ORCID] https://orcid.org/0000-0002-5845-7869
Erik Schäffer ![ORCID] https://orcid.org/0000-0001-7876-085X

REFERENCES

1. Hoyer, P., de Medeiros, G., Balázs, B., Norlin, N., Besir, C., Kräusslich, H.-G., Engelhardt, J., Sahl, S. J., Hell, S. W., & Hufnagel, L. (2016). Breaking the diffraction limit of light-sheet fluorescence microscopy by RESOLFT. *Proceedings of the National Academy of Sciences*, *113*(13), 3442–3446. http://www.pnas.org/lookup/doi/10.1073/pnas.1522292113.
2. Power, R. M., & Huisken, J. (2017). A guide to light-sheet fluorescence microscopy for multiscale imaging. *Nature Methods*, *14*(4), 360–373. http://www.nature.com/articles/nmeth.4224.
3. Olarte, O. E., Andilla, J., Gualda, E. J., & Loza-Alvarez, P. (2018). Light-sheet microscopy: A tutorial. *Advances in Optics and Photonics*, *10*(1), 111. https://www.osapublishing.org/abstract.cfm?URI=aop-10-1-111.
4. Chatterjee, K., Pratiwi, F. W., Wu, F. C. M., Chen, P., & Chen, B. C. (2018). Recent progress in light sheet microscopy for biological applications. *Applied Spectroscopy*, *72*(8), 1137–1169. http://journals.sagepub.com/doi/10.1177/0003702818778851.
5. Albert-Smet, I., Marcos-Vidal, A., Vaquero, J. J., Desco, M., Muñoz-Barrutia, A., & Ripoll, J. (2019). Applications of light-sheet microscopy in microdevices. *Frontiers in Neuroanatomy*, *13*, 1. https://www.frontiersin.org/article/10.3389/fnana.2019.00001/full.
6. Hanrahan, N., Lane, S. I. R., Johnson, P., Bourdakos, K., Brereton, C., Ridley, R. A., Davies, E. R., Hosny, N. A., Spickermann, G., Forster, R., Malcolm, G., Davies, D., Jones, M. G., & Mahajan, S. (2020). Label-free and multimodal second harmonic generation light sheet microscopy. bioRxiv, p. 2020.09.07.284703. https://doi.org/10.1101/2020.09.07.284703.
7. Remacha, E., Friedrich, L., Vermot, J., & Fahrbach, F. O. (2020). How to define and optimize axial resolution in light-sheet microscopy: A simulation-based approach. *Biomedical Optics Express*, *11*(1), 8.
8. Migliori, B., Datta, M. S., Dupre, C., Apak, M. C., Asano, S., Gao, R., et al. (2018). Light sheet theta microscopy for rapid high-resolution imaging of large biological samples. *BMC Biology*, *16*(1), 1–19.
9. Huisken, J., Swoger, J., Bene, F. D., Wittbrodt, J., & Stelzer, E. H. K. (2004). Optical sectioning deep inside live embryos by selective plane illumination microscopy. *Science*, *305*(5686), 13–16. http://science.sciencemag.org/content/305/5686/1007.
10. Keller, P. J., Schmidt, A. D., Wittbrodt, J., & Stelzer, E. H. K. (2011). Digital scanned laser light-sheet fluorescence microscopy (DSLM) of zebrafish and drosophila embryonic development. *Cold Spring Harbor Protocols 2011*, (10), pdb.prot065839–pdb.prot065839. http://www.cshprotocols.org/cgi/doi/10.1101/pdb.prot065839.
11. Hu, Y. S., Zimmerley, M., Li, Y., Watters, R., & Cang, H. (2014). Single-molecule super-resolution light-sheet microscopy. *ChemPhysChem*, *15*(4), 577–586.
12. Gustavsson, A. K., Petrov, P. N., & Moerner, W. E. (2018). Light sheet approaches for improved precision in 3D localization-based super-resolution imaging in mammalian cells [Invited]. *Optics Express*, *26*(10), 13122. https://www.osapublishing.org/abstract.cfm?URI=oe-26-10-13122.
13. Fahrbach, F. O., Simon, P., & Rohrbach, A. (2010). Microscopy with self-reconstructing beams. *Nature Photonics*, *4*(11), 780–785. http://doi.org/10.1038/nphoton.2010.204.
14. Planchon, T. A., Gao, L., Milkie, D. E., Davidson, M. W., Galbraith, J. A., Galbraith, C. G., et al. (2011). Rapid three-dimensional isotropic imaging of living cells using Bessel beam plane illumination. *Nature Methods*, *8*(5), 417–423. http://www.nature.com/articles/nmeth.1586.
15. Kashekodi, A. B., Meinert, T., Michiels, R., & Rohrbach, A. (2018). Miniature scanning light-sheet illumination implemented in a conventional microscope. *Biomedical Optics Express*, *9*(9), 4263. https://www.osapublishing.org/abstract.cfm?URI=boe-9-9-4263.
16. Gustavsson, A. K., Petrov, P. N., Lee, M. Y., Shechtman, Y., & Moerner, W. E. (2018). 3D single-molecule super-resolution microscopy with a tilted light sheet. *Nature Communications*, *9*(1), 123. http://www.nature.com/articles/s41467-017-02563-4.
17. Dunsby, C. (2008). Optically sectioned imaging by oblique plane microscopy. *Optics Express*, *16*(25), 20306. https://www.osapublishing.org/abstract.cfm?uri=ECBO-2009-7367_0H https://www.osapublishing.org/oe/abstract.cfm?uri=oe-16-25-20306.
18. Tokunaga, M., Imamoto, N., & Sakata-Sogawa, K. (2008). Highly inclined thin illumination enables clear single-molecule imaging in cells. *Nature Methods*, *5*(2), 159–161. http://www.nature.com/articles/nmeth1171.
19. Sapoznik, E., Chang, B. J., Huh, J., Ju, R. J., Azarova, E. V., Pohlkamp, T., et al. (2020). A versatile oblique plane microscope for large-scale and high-resolution imaging of subcellular dynamics. *eLife*, *9*, 1–39.
20. Fiolka, R. (2019). Resolution upgrades for light-sheet microscopy. *Nature Methods*, *16*(9), 813–814. http://doi.org/10.1038/s41592-019-0542-4.
21. Yang, B., Lange, M., Millett-Sikking, A., Solak, A. C., Kumar, S. V., Wang, W., Kobayashi, H., McCarroll, M. N., Whitehead, L.

W., Fiolka, R. P., Kornberg, T. B., York, A. G., & Royer, L. A. (2021). High-resolution, large imaging volume, and multi-view single objective light-sheet microscopy. bioRxiv. https://doi.org/10.1101/2020.09.22.309229

22. Kim, J., Wojcik, M., Wang, Y., Moon, S., Zin, E. A., Marnani, N., et al. (2019). Oblique-plane single-molecule localization microscopy for tissues and small intact animals. *Nature Methods*, *16*(9), 853–857.

23. Yang, B., Chen, X., Wang, Y., Feng, S., Pessino, V., Stuurman, N., et al. (2019). Epi-illumination SPIM for volumetric imaging with high spatial-temporal resolution. *Nature Methods*, *16*(6), 501–504. http://doi.org/10.1038/s41592-019-0401-3.

24. Galland, R., Grenci, G., Aravind, A., Viasnoff, V., Studer, V., & Sibarita, J. B. B. (2015). 3D high- and super-resolution imaging using single-objective SPIM. *Nature Methods*, *12*(7), 641–644. http://www.nature.com/doifinder/10.1038/nmeth.3402 http://www.ncbi.nlm.nih.gov/pubmed/25961414.

25. Meddens, M. B. M., Liu, S., Finnegan, P. S., Edwards, T. L., James, C. D., & Lidke, K. A. (2016). Single objective light-sheet microscopy for high-speed whole-cell 3D super-resolution. *Biomedical Optics Express*, *7*(6), 2219. https://www.osapublishing.org/abstract.cfm?URI=boe-7-6-2219.

26. Ponjavic, A., Ye, Y., Laue, E., Lee, S. F., & Klenerman, D. (2018). Sensitive light-sheet microscopy in multiwell plates using an AFM cantilever. *Biomedical Optics Express*, *9*(12), 5863. https://www.osapublishing.org/abstract.cfm?URI=boe-9-12-5863.

27. Hu, Y. S., Zhu, Q., Elkins, K., Tse, K., Li, Y., Fitzpatrick, JaJ., et al. (2013). Light-sheet Bayesian microscopy enables deep-cell super-resolution imaging of heterochromatin in live human embryonic stem cells. *Optical Nanoscopy*, *2*(1), 7. http://www.optnano.com/content/2/1/7.

28. Zagato, E., Brans, T., Verstuyft, S., van Thourhout, D., Missinne, J., van Steenberge, G., et al. (2017). Microfabricated devices for single objective single plane illumination microscopy (SoSPIM). *Optics Express*, *25*(3), 1732.

29. Gebhardt, J. C. M., Suter, D. M. D., Roy, R., Zhao, Z. W., Chapman, A. R., Basu, S., et al. (2013). Single-molecule imaging of transcription factor binding to DNA in live mammalian cells. *Nature Methods*, *10*(5), 421–426. http://www.pubmedcentral.nih.gov/articlerender.fcgi?artid=3664538&tool=pmcentrez&rendertype=abstract http://www.nature.com/nmeth/journal/v10/n5/abs/nmeth.2411.html.

30. Zhao, Z. W., Roy, R., Gebhardt, J. C. M., Suter, D. M., Chapman, A. R., & Xie, X. S. (2014). Spatial organization of RNA polymerase II inside a mammalian cell nucleus revealed by reflected light-sheet superresolution microscopy. *Proceedings of the National Academy of Sciences*, *111*(2), 681–686. http://www.pnas.org/content/111/2/681.short http://www.pnas.org/cgi/doi/10.1073/pnas.1318496111.

31. Greiss, F., Deligiannaki, M., Jung, C., Gaul, U., & Braun, D. (2016). Single-molecule imaging in living drosophila embryos with reflected light-sheet microscopy. *Biophysj*, *110*(4), 939–946. http://doi.org/10.1016/j.bpj.2015.12.035.

32. Fahrbach, F. O., Voigt, F. F., Schmid, B., Helmchen, F., & Huisken, J. (2013). Rapid 3D light-sheet microscopy with a tunable lens. *Optics Express*, *21*(18), 21010. https://www.osapublishing.org/abstract.cfm?URI=oe-21-18-21010.

33. Jiang, J., Zhang, D., Walker, S., Gu, C., Ke, Y., Yung, W. H., et al. (2015). Fast 3-D temporal focusing microscopy using an electri-

cally tunable lens. *Optics Express*, *23*(19), 24362. https://www.osapublishing.org/abstract.cfm?URI=oe-23-19-24362.

34. Cella Zanacchi, F., Lavagnino, Z., Perrone Donnorso, M., Del Bue, A., Furia, L., Faretta, M., et al. (2011). Live-cell 3D super-resolution imaging in thick biological samples. *Nature Methods*, *8*(12), 1047–1049. http://www.nature.com/articles/nmeth.1744.

35. Hermsdorf, G. L., Szilagyi, S. A., Rösch, S., & Schäffer, E. (2019). High performance passive vibration isolation system for optical tables using six-degree-of-freedom viscous damping combined with steel springs. *Review of Scientific Instruments*, *90*(1), 015113. https://doi.org/10.1063/1.5060707.

36. Sudhakar, S., Abdosamadi, M. K., Jachowski, T. J., Bugiel, M., Jannasch, A., & Schäffer, E. (2021). Germanium nanospheres for ultraresolution picotensiometry of kinesin motors. *Science*, *371*(6530), eabd9944. https://www.sciencemag.org/lookup/doi/10.1126/science.abd9944.

37. Simmert, S., Abdosamadi, M. K., Hermsdorf, G., & Schäffer, E. (2018). LED-based interference-reflection microscopy combined with optical tweezers for quantitative three-dimensional microtubule imaging. *Optics Express*, *26*(11), 14499. https://www.osapublishing.org/abstract.cfm?URI=oe-26-11-14499.

38. Mahamdeh, M., Simmert, S., Luchniak, A., Schäffer, E., & Howard, J. (2018). Label-free high-speed wide-field imaging of single microtubules using interference reflection microscopy. *Journal of Microscopy*, *272*(1), 60–66. http://doi.wiley.com/10.1111/jmi.12744.

39. Edelstein, A., Amodaj, N., Hoover, K., Vale, R., & Stuurman, N. (2010). Computer control of microscopes using uManager. *Current Protocols in Molecular Biology*, *92*, 1–17. http://doi.wiley.com/10.1002/0471142727.mb1420s92.

40. Angelova, M. I., Soléau, S., Méléard, P., Faucon, F., & Bothorel, P. (1992). Preparation of giant vesicles by external AC electric fields. Kinetics and applications. In Helm, C., Lösche, M. & Möhwald, H. (Eds.), *Trends in colloid and interface science VI* (Vol. 89, pp. 127–131). Steinkopff. https://doi.org/10.1007/BFb0116295.

41. García-Sáez, A. J., Ries, J., Orzáez, M., Pérez-Payà, E., & Schwille, P. (2009). Membrane promotes tBID interaction with BCLXL. *Nature Structural & Molecular Biology*, *16*(11), 1178–1185. http://doi.org/10.1038/www.nature.com/articles/nsmb.1671.

42. Unsay, J. D., Cosentino, K., & García-Sáez, A. J. (2015). Atomic force microscopy imaging and force spectroscopy of supported lipid bilayers. *Journal of Visualized Experiments*, *101*, e52867. http://www.jove.com/video/52867/atomic-force-microscopy-imaging-force-spectroscopy-supported-lipid.

43. Sudhakar, S., Jachowski, T. J., Kittelberger, M., Maqbool, A., Hermsdorf, G. L., Abdosamadi, M. K., et al. (2019). Supported solid lipid bilayers as a platform for single-molecule force measurements. *Nano Letters*, *19*(12), 8877–8886. https://pubs.acs.org/doi/10.1021/acs.nanolett.9b03761.

44. Schindelin, J., Arganda-Carreras, I., Frise, E., Kaynig, V., Longair, M., Pietzsch, T., et al. (2012). Fiji: An open-source platform for biological-image analysis. *Nature Methods*, *9*(7), 676–682. http://www.nature.com/articles/nmeth.2019.

45. Allan, D. B., Caswell, T., Keim, N. C., & van der Wel, C. M. (2018). trackpy: Trackpy v0.4.1. https://doi.org/10.5281/zenodo.1226458#.XFAkGVDbEVo.mendeley.

46. Przybylo, M., Sýkora, J., Humpolíčková, J., Benda, A., Zan, A., & Hof, M. (2006). Lipid diffusion in giant unilamellar vesicles is more than 2 times faster than in supported phospholipid bilayers

under identical conditions. *Langmuir*, *22*(22), 9096–9099. http://pubs.acs.org/doi/abs/10.1021/la061934p.

47. Michalet, X. (2010). Mean square displacement analysis of single-particle trajectories with localization error: Brownian motion in isotropic medium. *Physical Review E*, *82*, 041914.

48. Machá, R., & Hof, M. (2010). Lipid diffusion in planar membranes investigated by fluorescence correlation spectroscopy. *Biochimica et Biophysica Acta (BBA) - Biomembranes*, *1798*(7), 1377–1391. http://linkinghub.elsevier.com/retrieve/pii/S0005273610000544.

49. Quemeneur, F., Sigurdsson, J. K., Renner, M., Atzberger, P. J., Bassereau, P., & Lacoste, D. (2014). Shape matters in protein mobility within membranes. *Proceedings of the National Academy of Sciences*, *111*(14), 5083–5087. http://www.pnas.org/cgi/doi/10.1073/pnas.1321054111.

50. Koukourakis, N., Finkeldey, M., Stürmer, M., Leithold, C., Gerhardt, N. C., Hofmann, M. R., et al. (2014). Axial scanning in confocal microscopy employing adaptive lenses (CAL). *Optics Express*, *22*(5), 6025.

51. Chakraborty, T., Chen, B., Daetwyler, S., Chang, B. J., Vanderpoorten, O., Sapoznik, E., et al. (2020). Converting lateral scanning into axial focusing to speed up three-dimensional microscopy. *Light: Science and Applications*, *9*(1). http://doi.org/10.1038/s41377-020-00401-9.

52. Kang, S. Y., Duocastella, M., & Arnold, C. B. (2020). Variable optical elements for fast focus control. *Nature Photonics*, *14*(9), 533–542. https://www.nature.com/articles/s41566-020-0684-z.

53. Gu, M., & Sheppard, C. J. R. (1994). Effects of defocus and primary spherical aberration on images of a straight edge in confocal microscopy. *Applied Optics*, *33*(4), 625–630.

54. Reihani, S. N. S., Charsooghi, M. A., Khalesifard, H. R., & Golestanian, R. (2006). Efficient in-depth trapping with an oil-immersion objective lens. *Optics Letters*, *31*(6), 766–768.

55. Reihani, S. N. S., & Oddershede, L. B. (2007). Optimizing immersion media refractive index improves optical trapping by compensating spherical aberrations. *Optics Letters*, *32*(14), 1998–2000.

56. Iwai, D., Izawa, H., Kashima, K., Ueda, T., & Sato, K. (2019). Speeded-up focus control of electrically tunable lens by sparse optimization. *Scientific Reports*, *9*(1), 12365. https://doi.org/10.1038/www.nature.com/articles/s41598-019-48900-z.